Chemical Science

EDGE ARTICLE

View Article Online
View Journal | View Issue

Cite this: *Chem. Sci.*, 2019, **10**, 3701

All publication charges for this article have been paid for by the Royal Society of Chemistry

Topologically immobilized catalysis centre for long-term stable carbon dioxide reforming of methane†

Shusaku Shoji,[a] Xiaobo Peng,[*b] Tsubasa Imai,[c] Paskalis Sahaya Murphin Kumar,[d] Kimitaka Higuchi,[e] Yuta Yamamoto,[e] Tomoharu Tokunaga,[e] Shigeo Arai,[e] Shigenori Ueda,[bf] Ayako Hashimoto,[bg] Noritatsu Tsubaki,[h] Masahiro Miyauchi,[a] Takeshi Fujita[*i] and Hideki Abe[*bc]

Methane reforming at low temperatures is of growing importance to mitigate the environmental impact of the production of synthesis gas, but it suffers from short catalyst lifetimes due to the severe deposition of carbon byproducts. Herein, we introduce a new class of topology-tailored catalyst in which tens-of-nanometer-thick fibrous networks of Ni metal and oxygen-deficient Y_2O_3 are entangled with each other to form a rooted structure, *i.e.*, Ni#Y_2O_3. We demonstrate that the rooted Ni#Y_2O_3 catalyst stably promotes the carbon-dioxide reforming of methane at 723 K for over 1000 h, where the performance of traditional supported catalysts such as Ni/Y_2O_3 diminishes within 100 h due to the precluded mass transport by accumulated carbon byproducts. *In situ* TEM demonstrates that the supported Ni nanoparticles are readily detached from the support surface in the reaction atmosphere, and migrate around to result in widespread accumulation of the carbon byproducts. The long-term stable methane reforming over the rooted catalyst is ultimately attributed to the topologically immobilized Ni catalysis centre and the synergistic function of the oxygen-deficient Y_2O_3 matrix, which successfully inhibits the accumulation of byproducts.

Received 7th November 2018
Accepted 12th February 2019

DOI: 10.1039/c8sc04965c

rsc.li/chemical-science

Introduction

The catalytic conversion of the major component in biogas and natural gas, methane (CH_4), into valuable synthesis gas consisting of CO and H_2, is of increasing importance to establish a hydrogen-based society as well as for petroleum-free carbon resource management. Meanwhile, it is acknowledged that deposition of solid-state carbon byproducts (carbon deposition) is a significant drawback for CH_4 reforming.[1–9] In order to suppress carbon deposition, CH_4 reforming is currently conducted at high temperatures (>1073 K) and as a result, suffers from rapid catalyst degradation and huge energy consumption.[1–4] In contrast, CH_4 reforming at 873 K or lower temperatures may be favourable to mitigate the catalyst degradation and environmental impacts. However, the carbon deposition is strongly accelerated at low temperatures *via* CH_4 decomposition ($CH_4 = C(s) + 2H_2$) and/or CO disproportionation ($2CO = C(s) + CO_2$), which inhibits mass transport and shortens catalyst lifetime.[1,7–9] Although CO_2 dry reforming of CH_4 (DRM: $CH_4 + CO_2 = 2CO + 2H_2$) is highly promising among the different types of CH_4 reforming in terms of the efficient use of carbon feedstocks and the reduction of CO_2 emissions,[1,10–18] DRM is the most readily subjected to carbon deposition, especially at low temperatures. Recently, several strategies of designing core–shell structures and/or doping with other additive elements have been proposed to suppress undesirable carbon deposition,[19–29] yet it still remains a challenge.

Herein, we propose a material design strategy to preclude carbon deposition *via* tailoring the three-dimensional topology

[a]*Department of Materials Science and Engineering, School of Materials and Chemical Technology, Tokyo Institute of Technology, 2-12-1, Ookayama, Meguro-ku, Tokyo, 152-8552, Japan*

[b]*National Institute for Materials Science, 1-1 Namiki, Tsukuba, Ibaraki 305-004, Japan. E-mail: PENG.Xiaobo@nims.go.jp; ABE.Hideki@nims.go.jp*

[c]*Graduate School of Science and Technology, Saitama University, 255 Shimo-Okubo, Saitama 338-8570, Japan*

[d]*Anna University, Chennai, Tamil Nadu 600-025, India*

[e]*Institute of Materials and Systems for Sustainability, Nagoya University, Furo-cho, Chikusa-ku, Nagoya 464-8601, Japan*

[f]*Synchrotron X-ray Station at SPring-8, National Institute for Materials Science, 1-1-1 Kouto, Sayo, Hyogo, 679-5148, Japan*

[g]*Precursory Research for Embryonic Science and Technology, Japan Science and Technology Agency (JST), 4-1-8 Honcho, Kawaguchi, Saitama 332-0012, Japan*

[h]*Department of Applied Chemistry, School of Engineering, University of Toyama, 3190 Gofuku, Toyama 930-8555, Japan*

[i]*School of Environmental Science and Engineering, Kochi University of Technology, 185 Miyanokuchi, Tosayamada, Kami City, Kochi 782-8502, Japan. E-mail: fujita.takeshi@kochi-tech.ac.jp*

† Electronic supplementary information (ESI) available: Demonstration procedure; experimental and characterization details. See DOI: 10.1039/c8sc04965c

of metal/oxide nanocomposites. We demonstrate that a nanocomposite, consisting of entangled networks of tens-of-nanometre-thick fibrous phases of nickel metal and oxygen-deficient yttrium oxide, *i.e.*, Ni#Y_2O_3, can be prepared by utilizing nanophase-separation of a Ni–Y alloy in an oxidative atmosphere. The Ni#Y_2O_3 catalyst can activate CO_2 and CH_4 from a low temperature of 623 K (see Fig. S1†) and stably promote the DRM reaction at 723 K (low-temperature DRM; abbreviated as LT-DRM hereafter) for over 1000 h, whereas traditional supported catalysts such as Ni/Al_2O_3 and Ni/Y_2O_3 diminish the catalytic performance within 100 h. Advanced characterizations, including *in situ* transmission electron microscopy, elucidate that particle migration occurs in the supported catalysts in the reaction atmosphere, and the migrating metal nanoparticles act as a major catalyst centre for the widespread growth of fibrous carbon byproducts. However, the Ni catalysis centre of the Ni#Y_2O_3 catalyst is, like a tree deeply rooted in the ground, topologically immobilized by entanglement with the oxygen-deficient Y_2O_3 matrix, which can eliminate carbon byproducts to realize long-term stable DRM performance.

Results and discussion

The preparation processes for different metal/oxide catalysts are shown in Fig. 1. Traditional supported catalysts including Ni/Y_2O_3 and Ni/Al_2O_3 were prepared by a routine impregnation method (Fig. 1a; see the ESI† for details). The Ni#Y_2O_3 catalyst was obtained from a Ni–Y (Ni : Y = 1 : 1) alloy precursor consisting of Ni metal and oxyphilic Y metal (Fig. S2†). The Ni–Y alloy was heated at 873 K in a gas mixture of CO and O_2 (CO : O_2 = 2 : 1 in volume%; see details in the ESI†) to promote nanophase separation from a uniform alloy into a nanocomposite consisting of metal Ni and Y_2O_3, namely, Ni#Y_2O_3.

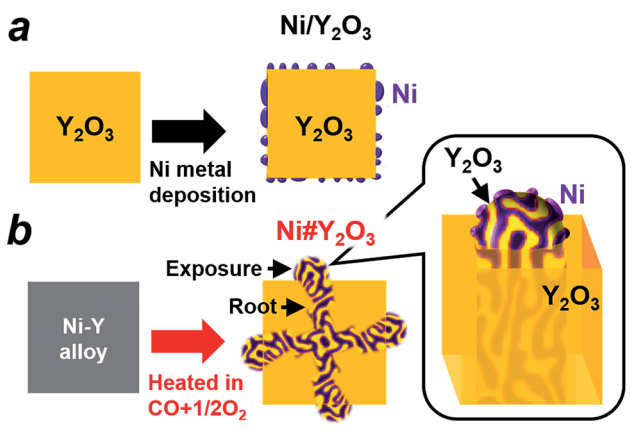

Fig. 1 Designing metal/oxide catalysts with different topologies. (a) Traditional supported catalysts such as Ni/Y_2O_3 are prepared by depositing Ni nanoparticles onto the support surface. (b) The rooted Ni#Y_2O_3 catalyst is prepared by (1) melting Ni and Y metals into a Ni–Y alloy in an Ar atmosphere and then (2) heating the prepared Ni–Y alloy in an atmosphere consisting of CO and O_2. A fibrous Ni phase is entangled with the Y_2O_3 counterpart and further rooted in the bulk (see the inset).

The Ni#Y_2O_3 nanocomposite comprised an entangled network of fibrous metal Ni and Y_2O_3, which further sprouted out of the bulk to develop a rooted structure (Fig. 1b; see Fig. S3† for a possible formation mechanism of the rooted structure).[30] As the control catalyst, different Ni–Y_2O_3 nanocomposites with different Ni/Y ratios of 5/1, 3/1, 2/1 and 1/3 were prepared from the corresponding Ni–Y alloy precursors (Ni_5Y, Ni_3Y, Ni_2Y and NiY_3, respectively; Fig. S4 and S5†) *via* the same atmospheric treatment as for the Ni#Y_2O_3.

The microstructure of the Ni#Y_2O_3 catalyst was characterized with a scanning electron microscope (SEM). A number of precipitates were observed on the surface of the Ni#Y_2O_3 particles (Fig. 2a). The cross-section SEM images demonstrated that the precipitates arose from the exposure of a rooted structure that propagated from the bulk to the surface (Fig. 2b). High-magnification SEM and STEM observations further showed that the rooted structure was composed of fibrous Ni- and Y_2O_3 phases (Fig. 2c and d, see also Fig. 1b and S6–S8†).

We tested the Ni#Y_2O_3 catalyst for LT-DRM in comparison to the other Ni-based catalysts prepared from different alloy precursors (Fig. 3a, see the corresponding SEM images in Fig. S5†). Pure Ni-powder exhibited very low activity, due to the low dispersion degree of the active Ni sites (Table S1 and Fig. S9†). The different Ni–Y_2O_3 composites also exhibited lower consumption- and formation rates than the Ni#Y_2O_3 catalyst. This should be attributed to the overgrowth of Ni or Y_2O_3 during the atmospheric processing of CO/O_2 (Fig. S5 and S9†). The CH_4- and CO_2 consumption rates over the Ni#Y_2O_3 catalyst were close to half the value of the CO- and H_2 formation rates, showing that the LT-DRM was promoted in a nearly stoichiometric pathway. We then evaluated the turnover frequency (TOF) of Ni#Y_2O_3 and the different Ni-based catalysts towards CH_4 conversion (*i.e.* TOF_{CH_4}, Table S2†).[31,32] The Ni#Y_2O_3

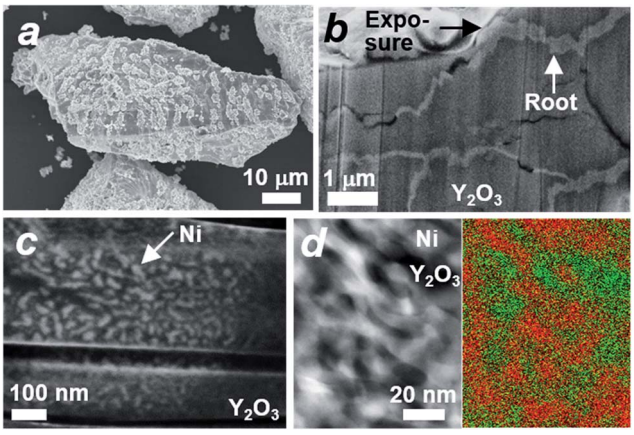

Fig. 2 Micro- and nanostructures of the rooted catalysts. (a) SEM image of one of the Ni#Y_2O_3 particles. (b) Cross-section SEM image of one of the Ni#Y_2O_3 particles, showing the distribution of the rooted structure in the bulk. The black arrow shows one of the exposures of the rooted structure. (c) High-magnification SEM image of the rooted structure shown in (b). (d) High-magnification HAADF STEM- (left) and elemental mapping images (right) of the rooted structure. The red- and green areas in the mapping image correspond to the Ni- and Y_2O_3 phases, respectively.

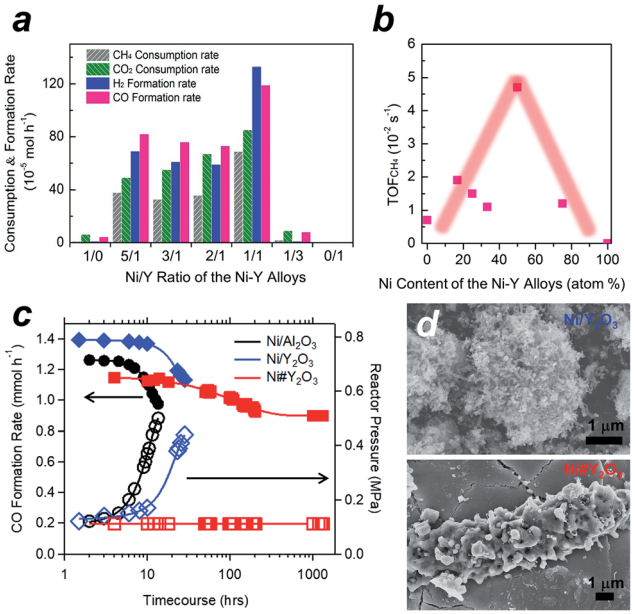

Fig. 3 LT-DRM performance of the Ni#Y_2O_3- and other Ni-based catalysts. Catalyst amount = 0.1 g; reaction temperature = 723 K; CH_4/CO_2/Ar = 1/1/98 in vol%; flow rate = 100 mL min^{-1}. (a) CO-/H_2 formation rates and CH_4-/CO_2 consumption rates for the Ni–Y_2O_3 composites with different Y contents. The Ni#Y_2O_3 corresponds to the Ni/Y ratio of the Ni–Y alloy = 1/1. (b) The turn-over frequencies (TOFs) towards CH_4 conversion over the Ni–Y_2O_3 composites with different Y contents. The Ni#Y_2O_3 corresponds to the Ni content of the Ni–Y alloy = 50%. (c) CO formation (left axis) and reactor pressure (right axis) for the Ni#Y_2O_3- and supported Ni catalysts. (d) SEM images of the Ni/Y_2O_3- and Ni#Y_2O_3 catalysts, 6 h after subjected to the LT-DRM atmosphere.

catalyst exhibited a much higher TOF_{CH_4} than the other catalysts prepared from different alloy precursors (Fig. 3b). The Ni#Y_2O_3 catalyst was optimized in terms of composition to achieve the highest LT-DRM performance.

We finally compared the Ni#Y_2O_3 catalyst with traditional supported catalysts in terms of long-term stability for LT-DRM (Fig. 3c). Note that the size of the Ni sites of Ni#Y_2O_3 (19 nm) was close to those of the supported catalysts including Ni/Y_2O_3 (19 nm) and Ni/Al_2O_3 (22 nm) (Table S1 and Fig. S10†). However, the Ni#Y_2O_3 catalyst stably promoted LT-DRM at 723 K for over 1000 hours, keeping the reactor pressure constant. A slight drop during the first 100 hours was observed, likely because the catalyst needed an initiation to reach a balance of carbon deposition and re-oxidation. In contrast, the traditional supported catalysts such as Ni/Al_2O_3 and Ni/Y_2O_3 showed rapid lowering in CO formation although they exhibited superior catalytic activity in the early stages.

A similar trend was also observed in dense gas conditions (Fig. S11;† catalyst amount = 0.1 g; reaction temperature = 823 K; CH_4/CO_2/N_2 = 10/10/5 in vol%; flow rate = 25 mL min^{-1}). The initial CH_4- and CO_2 conversions in LT-DRM were 49% and 38% over the supported Ni/Al_2O_3 catalyst, respectively, but rapidly decreased down to 12% and 9.1% after 10 h. However, our Ni#Y_2O_3 catalyst initially exhibited 12% and 20% for the CH_4- and CO_2 conversions, respectively, and kept them higher than 7.5% and 14% even at a time course of 100 h. The reactor pressure containing the supported catalysts increased as the conversion rates decreased, which was a typical trend observed when the reactor is clogged by carbon deposits (Fig. 3c and the inset in Fig. S11†). In addition, a higher TOF_{CH_4} was exhibited by the supported catalysts (Table S2†), but the carbon balance was much larger than unity (*i.e.* [CH_4 consumption rate + CO_2 consumption rate]/CO formation rate > 1.0; see Table S3† and the caption). The provided carbon species of CH_4 and/or CO_2 were more readily converted into carbon deposits than CO over the supported catalysts. Unlike the supported catalysts, Ni#Y_2O_3 exhibited a unity of carbon balance to achieve full conversion of CH_4 and CO_2 into CO without carbon deposits.

In order to elucidate the origin of the carbon-deposition tolerance of Ni#Y_2O_3, we performed different characterizations of the catalysts that were exposed to the LT-DRM atmosphere for 6 h (see Fig. S12† for pXRD). SEM observation showed that the supported Ni/Al_2O_3 as well as Ni/Y_2O_3 were heavily covered with fibrous deposits (Fig. 3d and S13†). The Ni#Y_2O_3 catalyst was free from fibrous deposits, instead it was thinly coated with a deposit layer (Fig. 3d and S14†). Raman analyses demonstrated that this deposited layer consisted of disordered and deficient carbon species (Fig. S15 and Table S4†).[33,34] In addition, hard X-ray photoemission spectroscopy (HAXPES: Fig. S16†) and thermogravimetry (TG: Fig. S17†) showed that the total amount of carbon deposits on the Ni#Y_2O_3 catalyst was less than that on the Ni/Al_2O_3- or Ni/Y_2O_3 catalysts.

We then conducted *in situ* TEM to shed light on the growth dynamics of the fibrous carbon in the LT-DRM atmosphere. The Ni/Al_2O_3 catalyst was exposed to a reactant gas consisting of equimolar CH_4 and CO_2 at 723 K with a pressure of 200 Pa, and observed with high-voltage *in situ* TEM (JEM-1000K RS TEM (JEOL), Nagoya Univ.). In an aliquot taken 2 h after the exposure to the reactant gas, an onion-shell pattern from graphitic carbon was clearly recognized all the way around the supported Ni nanoparticles (Fig. 4a). A series of *in situ* TEM snapshots

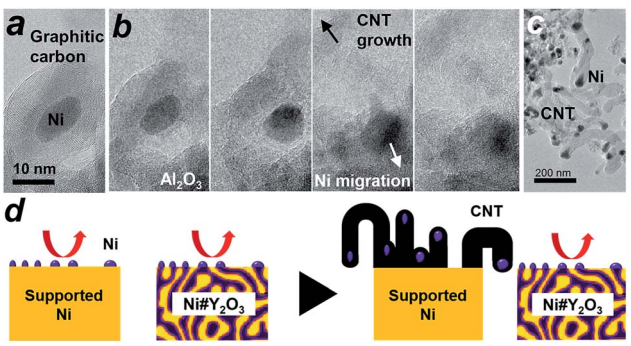

Fig. 4 Dynamic TEM observations of carbon deposition. (a and b) *In situ* TEM images visualizing the growth of fibrous carbon deposits (carbon nanotubes: CNT) over the Ni/Al_2O_3 catalyst in the LT-DRM atmosphere. Snapshots of the CNT growth. Shooting interval: ~2 seconds. (c) TEM image of the Ni/Al_2O_3 catalyst taken after subjection to LT-DRM for 6 h. (d) A model for the inhibited CNT growth over the Ni#Y_2O_3 catalyst due to the topological immobilization of the Ni catalysis centre.

show that this graphitic carbon layer was decomposed near at the Ni/Al_2O_3 interface, most likely by oxygen species donated from the Al_2O_3 support (Fig. 4b, see Movie S1†). The Ni nanoparticle in the field of view migrated away from the center to the bottom right through the missing part of the graphitic carbon layer.

Fig. 4b also shows that a rapid growth of hollow, multi-walled carbon nanotubes (CNT) was triggered by the migration of Ni nanoparticles. It is acknowledged that Ni nanoparticles, when they are able to freely migrate around without a support, play the role of an efficient catalyst that promotes the growth of long-length CNT fibres from gaseous carbon species such as ethanol vapour *via* a vapour–solid (VS) mechanism.[35–37] The carbon species provided from the gaseous atmosphere are dissolved in the Ni bulk and recrystallize on the surface in the form of a CNT, which further grows along with the drift of the migrating nanoparticles. As a result of collective migration of the Ni nanoparticles, the Ni/Al_2O_3 and Ni/Y_2O_3 catalysts were densely covered with large numbers of CNTs (50 nm and 500 nm in average thickness and length, respectively; Fig. 4c, S13 and S18†) after exposure to the LT-DRM atmosphere for 6 h. Note that each of the grown CNT contained one Ni nanoparticle at one end as the growth front.

By contrast to the supported Ni nanoparticles, the Ni catalyst centre of $Ni\#Y_2O_3$ is topologically immobilized due to entanglement with its Y_2O_3 counterpart, which can preclude particle migration and the accompanying CNT growth (Fig. 4d, see Fig. S19†). Moreover, the HAXPES results on the Ni 2p and O 1s regions showed that the Ni phase of $Ni\#Y_2O_3$ was retained as metal in the LT-DRM atmosphere, whereas the Ni phase of Ni/Y_2O_3 or Ni/Al_2O_3 was oxidized and/or carburized by CO_2 and/or CH_4 (Fig. S20 and S21†). The HAXPES spectra in the Y 3d region demonstrated that the Y_2O_3 phase of $Ni\#Y_2O_3$, unlike that of Ni/Y_2O_3, contained abundant oxygen vacancies (Fig. S22 and S23†).[38–40] The oxygen-deficient Y_2O_3 of $Ni\#Y_2O_3$ not only topologically immobilizes the Ni catalysis centre, but also may contribute to the elimination of carbon deposits *via* atomic exchange at the Ni–Y_2O_3 interface. In addition, the carbon deposits formed on the catalysis centre of $Ni\#Y_2O_3$ can be more readily oxidized than CNT or graphitic carbon because of their disordered and deficient nature (Fig. S15 and Table S4†).[1,41] Therefore, the rooted $Ni\#Y_2O_3$ catalyst, due to its topological advantages and the synergistic function with the oxygen-deficient Y_2O_3, successfully inhibited carbon deposition and improved reaction stability.

Conclusions

In conclusion, we present a catalyst design strategy that involves alloy preparations coupled with atmospheric processing to promote the spontaneous formation of nanocomposites consisting of entangled networks of metal and oxides. By tuning the composition of alloy precursors and the processing atmosphere, we have successfully built a composite catalyst with a rooted nanostructure, namely, $Ni\#Y_2O_3$. The $Ni\#Y_2O_3$ catalyst realized an improved activity and long-term stability to LT-DRM. *In situ* microscopic observations demonstrated that the carbon deposition occurring on traditional supported catalysts is attributable to the collective migration of metal nanoparticles. The catalysis centre of the $Ni\#Y_2O_3$ is topologically immobilized by its oxygen-deficient Y_2O_3 counterpart to preclude particle migration and inhibit carbon deposition. Finally, the material design strategy of rooted catalysts reported here is not limited to the specific conversion of methane, but can be used for a broad range of practical applications, in which stable yet active metal/non-metal interfaces play a central role in performance, such as electrode catalysts for fuel cells and/or secondary batteries.[42,43]

Conflicts of interest

There are no conflicts to declare.

Acknowledgements

This work was preliminarily supported by the JST CREST program (grant No. JPMJCR15P1) and the JST PRESTO program towards "Innovative Catalysts". We acknowledge support from the Advanced Characterization Nanotechnology Platform of the High Voltage Electron Microscope Laboratory of Nagoya University. This work was carried out by utilizing the facility of NIMS TEM Station and was supported by the Global Research Center for Environment and Energy based on Nanomaterials Science. The HAXPES measurements were performed under the approval of the NIMS Synchrotron X-ray Station (Proposal No. 2015B4605, 2016A4607, 2016B4600, 2017A4602, 2017B4605, 2018A4600). The authors wish to thank Dr Iida, Mr Takeda and Ms Nohara for their persistent assistance and/or fruitful discussions to accomplish this work.

Notes and references

1 D. Pakhare and J. Spivey, *Chem. Soc. Rev.*, 2014, **43**, 7813–7837.
2 L. Shi, G. H. Yang, K. Tao, Y. Yoneyama, Y. S. Tan and N. Tsubaki, *Acc. Chem. Res.*, 2013, **46**, 1838–1847.
3 S. Li and J. Gong, *Chem. Soc. Rev.*, 2014, **43**, 7245–7256.
4 J. W. Han, C. Kim, J. S. Park and H. Lee, *ChemSusChem*, 2014, **7**, 451–456.
5 D. San-José-Alonso, J. Juan-Juan, M. J. Illán-Gómez and M. C. Román-Martínez, *Appl. Catal., A*, 2009, **371**, 54–59.
6 M.-S. Fan, A. Z. Abdullah and S. Bhatia, *Appl. Catal., B*, 2010, **100**, 365–377.
7 J. R. Rostrupnielsen and J. B. Hansen, *J. Catal.*, 1993, **144**, 38–49.
8 S. Wang, G. Q. Lu and G. J. Millar, *Energy Fuels*, 1996, **10**, 896–904.
9 A. M. Gadalla and B. Bower, *Chem. Eng. Sci.*, 1988, **43**, 3049–3062.
10 S. C. Tsang, J. B. Claridge and M. L. H. Green, *Catal. Today*, 1995, **23**, 3–15.
11 A. W. Budiman, S. H. Song, T. S. Chang, C. H. Shin and M. J. Choi, *Catal. Surv. Asia*, 2012, **16**, 183–197.
12 S. M. Kim, P. M. Abdala, T. Margossian, D. Hosseini, L. Foppa, A. Armutlulu, W. V. Beek, A. Comas-Vives,

C. Copéret and C. R. Müller, *J. Am. Chem. Soc.*, 2017, **139**, 1937–1949.
13 T. Margossian, K. Larmier, S. M. Kim, F. Krumeich, A. Fedorov, P. Chen, C. R. Müller and C. Copéret, *J. Am. Chem. Soc.*, 2017, **139**, 6919–6927.
14 Z. Liu, D. C. Grinter, P. G. Lustemberg, T. D. Nguyen-Phan, Y. Zhou, S. Luo, I. Waluyo, E. J. Crumlin, D. J. Stacchiola, J. Zhou, J. C. Carrasco, H. B. Busnengo, M. V. Ganduglia-Pirovano, S. D. Senanayake and J. A. Rodriguez, *Angew. Chem., Int. Ed.*, 2016, **55**, 7455–7459.
15 Y. H. Hu and E. Ruckenstein, *Adv. Catal.*, 2004, **48**, 297–345.
16 Y. H. Hu and E. Ruckenstein, *Catal. Rev.*, 2002, **44**, 423–453.
17 D. Pakhare, C. Shaw, D. Haynes, D. Shekhawat and J. Spivey, *J. CO_2 Util.*, 2013, **1**, 37–42.
18 Y. Kathiraser, U. Oemar, E. T. Saw, Z. Li and S. Kawi, *Chem. Eng. J.*, 2015, **278**, 62–78.
19 S. Das, J. Ashok, Z. Bian, N. Dewangan, M. H. Wai, Y. Du, A. Borgna, K. Hidajat and S. Kawi, *Appl. Catal., B*, 2018, **230**, 220–236.
20 Y. Kathiraser, W. Thitsartarn, K. Sutthiumporn and S. Kawi, *J. Phys. Chem. C*, 2013, **117**, 8120–8130.
21 Z. Li, M. Li, Z. Bian, Y. Kathiraser and S. Kawi, *Appl. Catal., B*, 2016, **188**, 324–341.
22 Z. Li, S. Das, P. Hongmanorom, N. Dewangan, M. H. Wai and S. Kawi, *Catal. Sci. Technol.*, 2018, **8**, 2763–2778.
23 Z. Li and S. Kawi, *Catal. Sci. Technol.*, 2018, **8**, 1915–1922.
24 Z. Li, Z. Wang, B. Jiang and S. Kawi, *Catal. Sci. Technol.*, 2018, **8**, 3363–3371.
25 Z. Li, Y. Kathiraser and S. Kawi, *ChemCatChem*, 2015, **7**, 160–168.
26 Z. Li, Y. Kathiraser, J. Ashok, U. Oemar and S. Kawi, *Langmuir*, 2014, **30**, 14694–14705.
27 Z. Li, L. Mo, Y. Kathiraser and S. Kawi, *ACS Catal.*, 2014, **4**, 1526–1536.
28 Z. Li, B. Jiang, Z. Wang and S. Kawi, *J. CO2 Util.*, 2018, **27**, 238–246.
29 Z. Li and S. Kawi, *ChemCatChem*, 2018, **10**, 2994–3001.
30 T. Tanabe, T. Imai, T. Tokunaga, S. Arai, Y. Yamamoto, S. Ueda, G. V. Ramesh, S. Nagao, H. Hirata, S. Matsumoto, T. Fujita and H. Abe, *Chem. Sci.*, 2017, **8**, 3374–3378.
31 M. F. Mark and W. F. Maier, *J. Catal.*, 1996, **164**, 122–130.
32 G. L. Bezemer, J. H. Bitter, H. P. Kuipers, H. Oosterbeek, J. E. Holewijn, X. D. Xu, F. Kapteijn, A. Jos van Dillen and K. P. de Jong, *J. Am. Chem. Soc.*, 2006, **128**, 3956–3964.
33 A. C. Ferrari and J. Robertson, *Phys. Rev. B: Condens. Matter Mater. Phys.*, 2000, **61**, 14095–14107.
34 M. A. Pimenta, G. Dresselhaus, M. S. Dresselhaus, L. G. Cancado, A. Jorio and R. Saito, *Phys. Chem. Chem. Phys.*, 2007, **9**, 1276–1290.
35 R. T. K. Baker, M. A. Barber, P. S. Harris, F. S. Feates and R. J. Waite, *J. Catal.*, 1972, **26**, 51–62.
36 R. T. Yang and J. P. Chen, *J. Catal.*, 1989, **115**, 52–64.
37 J.-P. Tessonnier and D. S. Su, *ChemSusChem*, 2011, **4**, 824–847.
38 G. B. Sun, K. Hidajat, X. S. Wu and S. Kawi, *Appl. Catal., B*, 2008, **81**, 303–312.
39 P. Malacrida, H. G. S. Casalongue, F. Masini, S. Kaya, P. Hernández-Fernández, D. Deiana, H. Ogasawara, I. E. L. Stephens, A. Nilsson and I. Chorkendorff, *Phys. Chem. Chem. Phys.*, 2015, **17**, 28121–28128.
40 X. Huang, G. Xue, C. Wang, N. Zhao, N. Sun, W. Wei and Y. Sun, *Catal. Sci. Technol.*, 2016, **6**, 449–459.
41 P. Ferreira-Aparicio, M. Fernandez-Garcia, A. Guerrero-Ruiz and I. Rodríguez-Ramos, *J. Catal.*, 2000, **190**, 296–308.
42 W. Wang, C. Su, Y. Wu, R. Ran and Z. Shao, *Chem. Rev.*, 2013, **113**, 8104–8151.
43 M. R. Palacin, *Chem. Soc. Rev.*, 2009, **38**, 2565–2575.